

# Below Breakdown Streamer Discharges Triggered With the Photoelectric Effect: Electro-hydrodynamic Simulations of Pre-breakdown Electrons

Liam Keeley

Department of Physics, Colorado College, Colorado Springs, CO 80903

January 29, 2024

## Abstract

In my thesis, I numerically investigate leveraging the photoelectric effect to trigger streamer formation in a spark gap. Specifically, we consider directing UV-light onto the cathode of a spark gap to induce the photoelectric effect. Then, because the photoelectric effect provides an electron source with no corresponding positive ions, we expect a negatively charged electron cloud to form in the gap, acting to reinforce the applied field near the anode. Thus, if we hold the applied field just below the breakdown threshold of the spark gap, we expect to trigger the spark gap when we direct UV-light onto the cathode. I use finite difference methods to simulate a fluid description of the pre-breakdown electron dynamics of the proposed UV-light triggered spark gap. Despite significant numerical error, the simulation confirms the working principle. I also use the simulation to investigate a number of pulse widths and discuss how the distribution of UV-light on the cathode effects the trigger mechanism.

## 1 Introduction

Spark gaps are used as high voltage pulse generators with applications in the development of fusion technologies and pulsed laser systems. In general, a spark gap is formed by applying a high voltage across two electrodes held in air. If we imagine a single free electron between the electrodes, then we can see that the electron will be accelerated by the applied field, collide with molecules in air and lose momentum, and then be accelerated by the field again. In some cases, the electron will travel far enough between collisions that it has kinetic energy greater than the ionization energy of the molecule: then, the electron can ionize that molecule. After such a collision, there will be two free electrons in the gas which can each ionize more molecules, but this collision also results in an ion which the electrons can reattach to in future collisions. If the rate that collisions cause air molecules to be ionized exceeds the rate that collisions cause electrons to reattach to ions, then a plasma known as a streamer will grow; otherwise, the streamer will be quenched. Because the ionization and recombination rates are related to the applied electric field, there is a specific electric field magnitude above which a streamer discharge will grow and below which it will not. This electric field is called the breakdown field of the spark gap.

The reliance of a spark gap on a single seed electron often results in a timing jitter (i.e. the uncertainty in the time between subsequent discharges) which is unsuitable for many applications.

In these cases, it is desirable to have a trigger mechanism: in this thesis, I investigate using the photo-electric effect to flood a spark gap with electrons to increase the consistency of discharges. When we consider many seed electrons, streamer formation becomes more complicated. In some cases, the presence of many seed electrons can cause a streamer discharge even when the applied electric field is below breakdown. For example, Sun et al. [1] used a Particle In Cell simulation to show that a discharge can occur below breakdown in the presence of a high density parcel of seed ionization. Because this parcel has many free charges, it acts as an ideal conductor: the charges will position themselves to screen the applied field inside the parcel of ionized gas. This redistribution of charge results in the field being enhanced at the parcel's edges: in Sun et al.'s simulation, a streamer grew from points where the field was locally above breakdown even when the applied field was below breakdown.

Rather than a seed ionization, the photoelectric effect in the UV-light triggered spark gap we are considering provides an external source of electrons. I expect the external source of electrons to form a cloud which will perturb the electric field, reinforcing it near the anode; similar to Sun et al.'s results, a streamer can grow from points where the local field exceeds the breakdown field. For this reason, we focus on the electron dynamics before breakdown to demonstrate the specifics of how we can trigger streamer discharges.

To study the behavior of released electrons prior to breakdown, I use fluid electro-hydrodynamics in 2D axisymmetric coordinates. In this regime, we assume that enough electrons are released so that fluid models can be used and the random motion of individual electrons is unimportant. We also assume that forces due to magnetic fields and pressure differentials are negligible; prior to breakdown, there is no reason that either of these forces would be comparable to the applied electrostatic force. In fact, even after breakdown magnetic forces are generally insignificant [2]. Finally, we assume symmetry so that the electron density, electron drift velocity, and electric potential functions are all axisymmetric about an axis running through the center of each electrode. Thus, the inherently 3D process can be modelled in 2D rz-coordinates, significantly decreasing the computational difficulty of the problem.

With these assumptions in mind, describing the electron dynamics reduces to solving the following coupled partial differential equations. First, Poisson's Equation of electrostatics is used to resolve the electric potential everywhere given the electron density function. Then, once the electric potential is resolved, the Electron Momentum Equation is used to describe the electron drift velocity. Finally, the Electron Continuity Equation is used to update the electron density. By iteratively solving these three equations using finite difference methods, we can move our simulation forward in time and explore whether conditions for below breakdown streamer discharges can be achieved in a UV-light triggered spark gap.

## 2 The Dynamical Equations of Motion

We will now develop the Continuity Equation and the Particle Momentum Equation from first principles, which ultimately will be used to simulate the motion of the pre-breakdown electron cloud. To highlight the generality of these equations, we will consider a general charged fluid acted upon by some electric field rather than the electron cloud we will ultimately apply the results to<sup>1</sup>.

---

<sup>1</sup>In this section, index notation will be used for brevity, and Cartesian coordinates will be used for simplicity. Terms with repeated indices imply a sum over all coordinates: for example, the dot product of two vectors  $\mathbf{A}$  and  $\mathbf{B}$

## 2.1 The Continuity Equation

We begin by deriving the continuity equation. The continuity equation is fundamentally a statement about any quantity which is locally conserved<sup>2</sup>; we are specifically interested in the particle number density. Consider a fixed volume  $V$  in which the number density is  $n = n(t, x, y, z)$ : if we integrate the number density over this volume, we get the total number of particles  $N$  in the volume:

$$N = \int_V n dV$$

The rate of change of  $N$  in our volume is then:

$$\frac{dN}{dt} = \frac{d}{dt} \int_V n dV = \int_V \partial_t n dV \quad (1)$$

Next, we assume local conservation of the particle number so that no particles are created or destroyed inside our volume. Then, the number of particles inside the volume can only change if particles pass across the boundary of the volume. To describe the number of particles passing over the boundary, we introduce the drift velocity  $u_i = u_i(t, x, y, z)$ , which describes the average velocity of particles in the fluid. While at the microscopic scale, each individual atom moves with a thermal velocity which is randomly distributed, the drift velocity measures the average velocity of many particles in a region sufficiently small we can treat it as infinitesimal (yet large enough we can treat it as continuous). If we mark off a small fluid parcel, the drift velocity describes how its position changes in time, or stated mathematically:  $u_i = \partial_t x_i$ . Using this definition, and our assumption of local conservation of particle number, we can describe the number of particles crossing the bounding surface  $\partial V$  of our volume as:

$$\left. \frac{dN}{dt} \right|_{\partial V} = - \oint_{\partial V} n u_i dA_i \quad (2)$$

Because particle number is conserved inside the volume, this is the rate of change of the number of particles inside the volume as well. Thus, we can equate Equation (1) and Equation (2):

$$\begin{aligned} \int_V \partial_t n dV &= - \oint_{\partial V} n u_i dA_i \\ \int_V \partial_t n dV + \oint_{\partial V} n u_i dA_i &= 0 \\ \int_V \partial_t n + \partial_i(n u_i) dV &= 0 \end{aligned}$$

Where the Divergence Theorem was used in the last step. This integral must be satisfied for any volume in which the particle number is locally conserved, which we assume to be everywhere in our domain. If the integral statement were satisfied but the integrand  $\partial_t n + \partial_i(n u_i)$  were *not* 0 somewhere in the volume, then the integrand would also have to be nonzero at least one other place in the volume so that the total integral were still 0. Because we took  $V$  to be arbitrary, we can define a new volume around one of these points in which the integral would be nonzero, contradicting our assumption of local conservation. We then conclude that the integrand must vanish:

---

will expressed  $A_i B_i = A_x B_x + A_y B_y + A_z B_z = \mathbf{A} \cdot \mathbf{B}$ . Partial derivatives will be expressed in subscript notation so that  $\partial_t = \frac{\partial}{\partial t}$  and  $\partial_i = \frac{\partial}{\partial x_i}$ : for example, the divergence of a vector  $\mathbf{A}$  will be expressed  $\partial_i A_i = \frac{\partial A_x}{\partial x} + \frac{\partial A_y}{\partial y} + \frac{\partial A_z}{\partial z} = \nabla \cdot \mathbf{A}$ .

<sup>2</sup>This derivation follows one given in Chapter 6 of [3]

$$\partial_t n + \partial_i(n u_i) = 0 \quad (3)$$

Which is the Continuity Equation. It is a kinematical equation, and in that regard is important in describing the motion of the electron cloud, but it tells us nothing about what causes that motion. To describe the motion, we need an equation akin to Newton's Second Law for a fluid, a problem which we turn to next.

## 2.2 The Particle Momentum Equation: Forces, Friction, and Newton's Second Law

To derive the Particle Momentum Equation – which describes how a fluid acted upon by a number of forces moves, stretches, and deforms – we use Newton's Second Law. The main challenge in applying Newton's Second Law to a fluid is that the shape and volume of a fluid material are not necessarily fixed in time. To account for this, consider a small parcel of fluid moving with the particle drift velocity everywhere. Although the bounding surface and the physical volume of this parcel are not fixed, we will assume the mass of the material is<sup>3</sup>. Each component of the total momentum of this fluid element is then:

$$p_i = \int_{\delta V(t)} u_i \rho dV$$

Where  $\delta V(t)$  is the volume occupied by the fluid parcel at time  $t$ . To apply Newton's Second Law to this parcel we must determine how to compute  $\frac{dp_i}{dt}$ . The integral changes in time because of both changes to the integrand  $u_i \rho$  as well as changes to the shape and volume of  $\delta V$ . From the definition of an integral as a sum of infinitesimal volume elements:

$$\begin{aligned} \frac{dp_i}{dt} &= \frac{d}{dt} \int_{\delta V(t)} u_i \rho dV = \frac{d}{dt} \lim_{n \rightarrow \infty} \sum_n [u_{in} \rho_n \delta V_n] \\ &= \lim_{n \rightarrow \infty} \sum_n \left[ \frac{d}{dt} (u_{in} \rho_n) \delta V_n + u_{in} \rho_n \frac{d \delta V_n}{dt} \right] \end{aligned}$$

The parcel volume  $\delta V$  changes shape because of the average motion of particles on its boundary  $\delta \vec{A}$ . So:

$$\frac{d \delta V_n}{dt} = \int_{\partial(\delta V)} u_j dA_j = \int_{\delta V} \partial_j u_j dV$$

Where the Divergence Theorem was used in the last step. It follows that:

$$\begin{aligned} \frac{dp_i}{dt} &= \lim_{n \rightarrow \infty} \sum_n \left[ \frac{d(u_{in} \rho_n)}{dt} + u_{in} \rho_n \int_{\delta V_n} \partial_j u_j dV \right] \\ &= \int_{\delta V} \frac{d(u_i \rho)}{dt} dV + \int_{\delta V} u_i \rho \partial_j u_j dV \end{aligned}$$

We can continue to simplify this. First, note that  $u_i \rho$  is a function of time and space coordinates. So, using the chain rule:

---

<sup>3</sup>This is not the only option; for instance, we could assume the volume of the parcel is constant but the mass of the material is not. See pp. 135 of [11].

$$\frac{d(u_i\rho)}{dt} = \partial_t(u_i\rho) + \partial_t x_j \partial_j(u_i\rho) = \partial_t(u_i\rho) + u_j \partial_j(u_i\rho)$$

We can recast this in terms of the convective derivative which is defined as  $\frac{D}{Dt} = \partial_t + u_i \partial_i$ . The convective derivative is the rate of change of some quantity measured while moving along with the fluid. In this case, we measure how the momentum of a specific parcel of fluid changes in time: it can move, wharp, disperse, or condense, and the convective derivative measures how the total momentum of the parcel is changing in the parcel's own frame. Then:

$$\begin{aligned} \frac{dp_i}{dt} &= \int_{\delta V} \frac{D(u_i\rho)}{Dt} dV + \int_{\delta V} u_i \rho \partial_j u_j dV \\ &= \int_{\delta V} \rho \frac{Du_i}{Dt} + u_i (\partial_t \rho + u_j \partial_j \rho) + u_i \rho \partial_j u_j dV \\ &= \int_{\delta V} \rho \frac{Du_i}{Dt} + u_i [\partial_t \rho + \partial_j(u_j \rho)] dV \end{aligned}$$

The bracketed term is a continuity equation, so by conservation of mass:

$$\frac{dp_i}{dt} = \int_{\delta V} \rho \frac{Du_i}{Dt}$$

Now, we can apply Newton's Second Law to the parcel. Specifically, we make a distinction between forces  $F_j$  which act on the fluid everywhere and stress energy forces, which we can represent with the pressure tensor<sup>4</sup>, and act only on the bounding surface of the parcel:

$$\begin{aligned} \int_{\delta V} \rho \frac{Du_j}{Dt} &= \int_{\delta V} F_j dV - \int_{\partial(\delta V)} P_{ij} dA_i \\ &= \int_{\delta V} F_j dV - \int_{\delta V} \partial_i P_{ij} dV \end{aligned}$$

Where the Divergence Theorem was used on the surface integral. Regardless, this must be applicable to any parcel  $\delta V$ , so applying the same argument used for the continuity equation, we conclude:

$$\rho \frac{Du_j}{Dt} = F_j - \partial_i P_{ij} \quad (4)$$

Which is the Particle Momentum Equation for a general fluid.

For our specific case of an electron cloud,  $F_j$  represents the electrostatic force<sup>5</sup> and a drag force caused by electrons colliding with neutral atoms. Additionally, pressure differentials are taken to be negligible with respect to the electrostatic force, so the pressure term vanishes. Finally, rather than tracking a separate mass density and charge density, we relate each to the particle number density  $n$ . If each electron has a mass  $m_e$  and a charge  $e$ , then the mass density is  $\rho = mn$  and the charge density is  $\rho_c = en$ . The Electron Momentum Equation we end up simulating is then:

$$m_e n \frac{Du_j}{Dt} = -enE_j - \nu_{en} m_e n u_j \quad (5)$$

Where  $\nu_{en}$  is the collision frequency between neutral atoms and electrons.

---

<sup>4</sup>In fluid mechanics, this is generally referred to as the stress energy tensor, not the pressure tensor. In plasma physics it is more often referred to as the pressure tensor which is the terminology we will use.

<sup>5</sup>Recall that we are assuming magnetic forces are negligible.

### 3 Simulation

We now use the models developed in Section 2 to investigate the problem of triggering a spark gap using a pulse of UV-light. This system of partial differential equations has no solutions in general, so I have developed a numerical framework based on finite difference methods to simulate the solution<sup>6</sup>. As we will find, the numerical error in our simulation framework is significant<sup>7</sup>, so we are unable to make sound quantitative conclusions. However, we are able to confirm that the electric field will be reinforced near the anode and provide insight into the design of a spark gap. We also discuss how these results compare with preliminary experiments we have conducted on a physical spark gap.

#### 3.1 Computational Domain, Boundary Conditions, and Choice of Physical Parameters

Here, we motivate the simulation parameters we use in our simulations. Because of the high numerical error in our simulation, we use back-of-the-envelope calculations to determine boundary conditions and physical parameters rather than attempting to be more exact than our framework allows. These methods allow for conceptually valid results, but a more exact simulation would also require complicated methods to determine boundary conditions and extensive calculations and empirical data to determine physical parameters.

We define our computational domain to extend from the surface of the cathode to the surface of the anode in the axial direction and well beyond the edge of the electrodes in the radial direction. This domain is then decomposed into an  $N \times N$  uniform grid: the electric potential, electron density, and electron velocity are tracked at each gridpoint as the simulation evolves in time. To conform with spark gap experiments we have conducted in the laboratory, we choose both the radius of the electrodes and the distance between electrodes to be 1 mm.

These definitions allow us to define boundary conditions. Each electrode is taken to be at a constant potential extending to the electrode edge after which the potential logarithmically approaches zero at large  $r$  as shown in Figure 1. The logarithmic decay of the potential is what we would expect from an infinite line charge. While the edge of the electrodes lack the symmetry of an infinite line charge, we use this as a reasonable starting place as a detailed treatment of the electrodes is hard. We take the total gap voltage to be  $\Delta V = 1000$  V. Using a parallel plate approximation, we can see this will result in an applied electric field of:

$$E \approx \frac{V}{d} = \frac{1000V}{1 \times 10^{-3}m} = 1 \times 10^6 \frac{V}{m}$$

Which is near the breakdown field of air at atmospheric pressure<sup>8</sup>.

The electron number density and drift velocity are governed by the nature of incident light on the cathode and of the cathode material. We assume light is incident in a Gaussian beam of  $E_\nu = 4.5$  eV photons ( $\lambda = 275$  nm). Then, we assume a total of  $10^{19} s^{-1}$  photons are incident on the cathode

---

<sup>6</sup>The details of this framework are discussed in Appendix A. Code is available in the project code repository.

<sup>7</sup>Streamer simulations generally struggle to achieve numerically sound results; see Bagheri et. Al. [9] for a discussion of the discrepancies found in several streamer simulation codes.

<sup>8</sup>See [12]. The breakdown field is usually going to be a little greater than  $1 \times 10^6 \frac{V}{m}$ ; however, because the electric potential in the parallel plate approximation used here decreases uniformly, the maximum field in our gap, where the potential does not decrease uniformly, will also exceed  $1 \times 10^6 \frac{V}{m}$ .

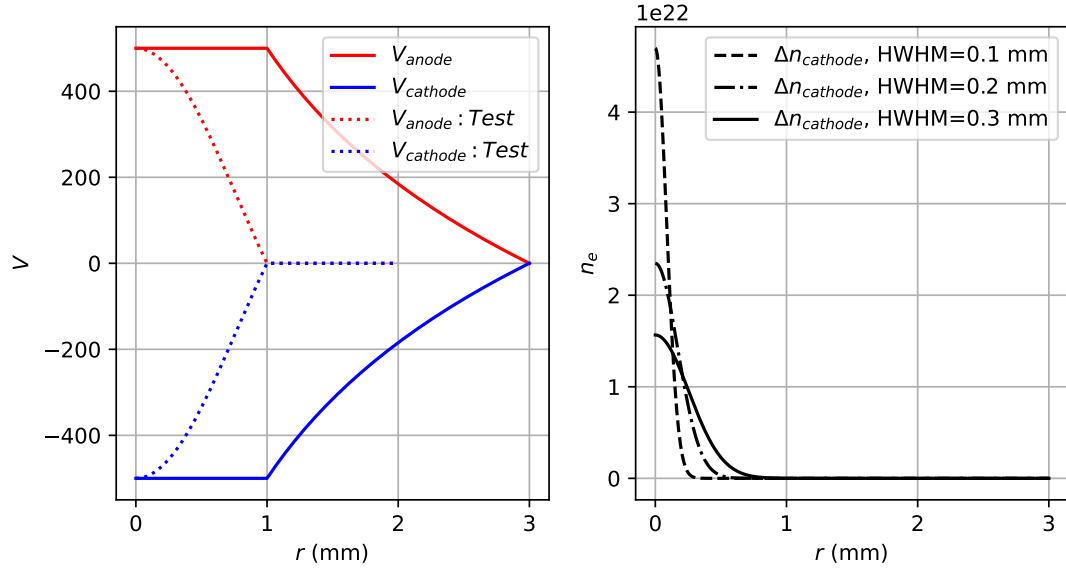


Figure 1: On the left, we show the boundary conditions used to represent the electrodes in our simulations. For error quantification and testing of our simulation framework, we use Bessel functions for the electrodes. In other simulations, we approximate physical electrodes extending to  $r = 1$  mm as being held at constant potential; then, the potential decays logarithmically to  $V = 0$  at large  $r$ . This scheme, which models the potential outside an infinitely long wire, is inaccurate for real electrodes, but provides a reasonable starting point. On the right, we show the boundary conditions used to model the electron density at the cathode. We take the electron density to be Gaussian at the cathode which approximates photo-electrons emitted due to a Gaussian UV-light beam. We simulate three boundaries, all with a total of  $N = 10^{19} s^{-1}$  electrons available at the cathode but with different width parameters.

per second, which is equivalent to a power output of  $P = \frac{NE}{\Delta t} \approx 7$  W, which is reasonable for a UV-LED in pulsed operation.

We assume that each photon releases an electron<sup>9</sup>, and so we take the total number of electrons available at the cathode to be  $10^{19} s^{-1}$ . We take the distribution of those electrons to be Gaussian, and investigate a number of width parameters as shown in Figure 1. We determine the velocity of electrons at the cathode from the conservation of energy condition:

$$\frac{1}{2}m_e v_0^2 = E_\nu - \phi$$

Where  $m_e$  is the electron mass and  $\phi$  is the work function of the metal used for the cathode. Taking  $\phi = 4$  eV<sup>10</sup>, we find:

$$v_0 = \sqrt{\frac{2}{m_e}(E_\nu - \phi)} \quad (6)$$

$$v_0 \approx 10^5 \text{ m/s} \quad (7)$$

The initial velocity will be essentially parallel to the cathode surface, or directly in the axial direction if the cathode is flat.

Next, we choose an appropriate electron-neutral collision frequency,  $\nu_{en}$ . To do this, we assume each electron scatters off of a static collection of neutrals so that<sup>11</sup>:

$$\nu_{en} = \sigma n_n v$$

Where  $\sigma$  is the electron neutral collision cross-section,  $n_n$  is the neutral number density, and  $v$  is the electron thermal velocity. We then assume the air is at standard pressure ( $P = 10^5$  Pa) and standard temperature ( $T_n = 300$  K). With these assumptions, we use the Ideal Gas Law to determine the neutral number density to be:

$$n_n = \frac{P}{kT} \approx 10^{25} \text{ m}^{-3}$$

The velocity of an electron in thermal equilibrium with the air will be:

$$v = \sqrt{\frac{2kT}{m_e}} \approx 10^5 \text{ m/s}$$

Which is the same as the velocity of a photo-electron, so taking  $v = 10^5 \text{ m/s}$  for a typical electron in the spark gap is reasonable. Finally, because there are no long range electromagnetic forces between electrons and neutrals, the collision cross section will be roughly that of an atomic radius:

$$\sigma = 10^{-20} \text{ m}^2$$

Putting this altogether, we find that:

$$\nu_{en} = \sigma n_n v \approx 10^{10} / \text{s} \quad (8)$$

Completing the parametrization of our simulation.

---

<sup>9</sup>This is unrealistic. A more careful treatment would be difficult because of the high applied field; the emission will be fundamentally different compared to photo-emission with no applied electric field. See [13].

<sup>10</sup>Which is roughly the work function of a typical metal such as aluminum.

<sup>11</sup>See Chapter 1 of [4] (and Chapter 13 for a detailed description of collisions).

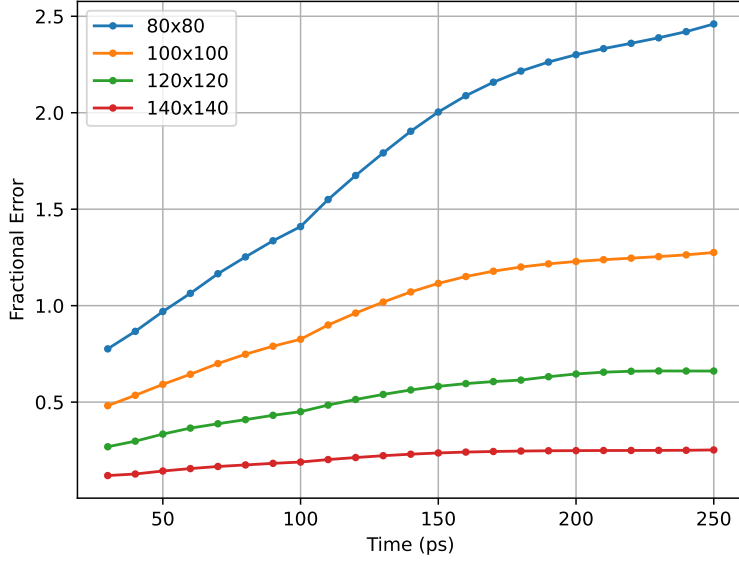


Figure 2: Estimated fractional error computed by comparing the total number of electrons  $N_e$  in solutions computed on various grids. Comparisons are made to the solution on a  $160 \times 160$  grid. Bessel functions were used to describe the potential at each electrode rather than the more realistic boundaries in other simulations. Generally, we encounter large errors, making it difficult to draw sound quantitative conclusions.

### 3.2 Error Analysis

Any numerical solution to a differential equation will have error, and the amount of error in the solution constrains how much physics we can learn from the solution. So, before discussing the results of our simulation, we must understand how much error we accrue.

We quantify the error in our solution by simulating the problem described by the boundary conditions in Figure 1 on  $N \times N$  grids of size  $80 \times 80$ ,  $100 \times 100$ ,  $120 \times 120$ ,  $140 \times 140$ , and  $160 \times 160$ . Then, we compute the total number of electrons  $N_e$  in the simulation at a time  $t$  as:

$$N_e = \int_V n dV \approx \sum_l^N \sum_j^N n_{j,l} \Delta z \pi \left[ (r_{j,l} + \frac{\Delta r}{2})^2 - (r_{j,l} - \frac{\Delta r}{2})^2 \right] \quad (9)$$

And we use  $N_e$  to compare solutions on various grids. In principle, this criterion fails for a distribution with the same number of electrons but a different distribution of those electrons. However, the shape of the solution is consistent across grids, so discrepancies in  $N_e$  will accurately represent error in the solution. The main advantage of using  $N_e$  to describe numerical error is that we avoid directly comparing cells of different sizes across grids. We compare the largest grid of size  $160 \times 160$  to each of the smaller grids by computing:

$$\delta N = \frac{|N_{160 \times 160} - N_{N \times N}|}{N_{160 \times 160}} \quad (10)$$

Figure 2 shows the time evolution of the estimated fractional error for each grid smaller than

$160 \times 160$  (as computed by comparing to the  $160 \times 160$  grid). Even though we do seem to be converging to an answer, the amount of error is high: even as high as %25 for the  $140 \times 140$  grid. This implies that the  $160 \times 160$  grid likely has significant error as well, although we cannot estimate it without an even larger grid<sup>12</sup>. Because of the error inherent in our solution, we cannot make sound numerical conclusions; however, especially considering that the general behavior of the electron cloud is consistent across grid size, we can use our simulation to gain qualitative insights into the triggering of a spark gap.

### 3.3 Results

Although any simulations we conduct will be quantitatively inaccurate, we conduct a number of simulations which provide important qualitative insights into the design of a spark gap. First, we confirm that an electron cloud formed by photo-electrons can reinforce the electric field by a sufficient amount to trigger a spark gap held just below its breakdown voltage. Then, keeping the total power of photons incident on the cathode constant, we explore how various pulse widths effect the electric field perturbation and the density of electrons near the anode.

Figure 3 shows the simulated behavior of electrons as well as the electric field perturbation due to those electrons (excluding the region by the cathode) in a 1 mm gap for a pulse width of HWHM = 0.2 mm. At  $t = 0$ , electrons begin to be released from the cathode; acted upon by the applied electric field, they move across the gap, reaching the anode in  $\sim 120$  ps. The electron number density falls off quickly with distance from the cathode, and is roughly  $\sim 10^{15}$  near the anode once a steady state is reached. We find that the greatest perturbation moves across the gap with the head of the electron cloud, and is greatest at the anode once a steady state is reached. So, when the cloud reaches the anode and then reaches a steady state, many electrons will be available to seed a discharge and the perturbation will be in the direction of the applied electric field. A discharge can be triggered if the perturbation is large enough to cause the breakdown voltage to be exceeded, which depends on how closely the gap can be held to its breakdown voltage and the magnitude of the electric field perturbation.

Despite the exact magnitude of the electric field being uncertain due to numerical error, the magnitude of  $\Delta E \approx 5000 \frac{V}{m}$  found in our simulations is in agreement with the preliminary physical experiments we have conducted. In these experiments, we succeeded in triggering a 1 mm spark gap held just below its breakdown voltage occasionally but not consistently using a pulse of UV-light from a UV-LED [7]. The voltage source we used had a resolution of  $\delta V = 10$  V; again using the parallel plate approximation, we can conclude that the uncertainty in the applied electric field was roughly:

$$\delta E = \frac{\delta V}{d} = \frac{10V}{10^{-3}m} = 10000 \frac{V}{m}$$

It follows that if the electric field perturbation caused the electron cloud is only  $\Delta \vec{E} \approx 5000 \frac{V}{m}$ , then breakdown voltages will sometimes be exceeded, but this will not occur consistently, as we have observed in physical experimentation. To achieve a consistent trigger mechanism, it appears that

---

<sup>12</sup>Although in principal we could continue to decrease the numerical error by simulating on larger and larger grids, in practice this is impractical as larger grids take longer to simulate. See Appendix A for a discussion of the computational complexity of this problem.

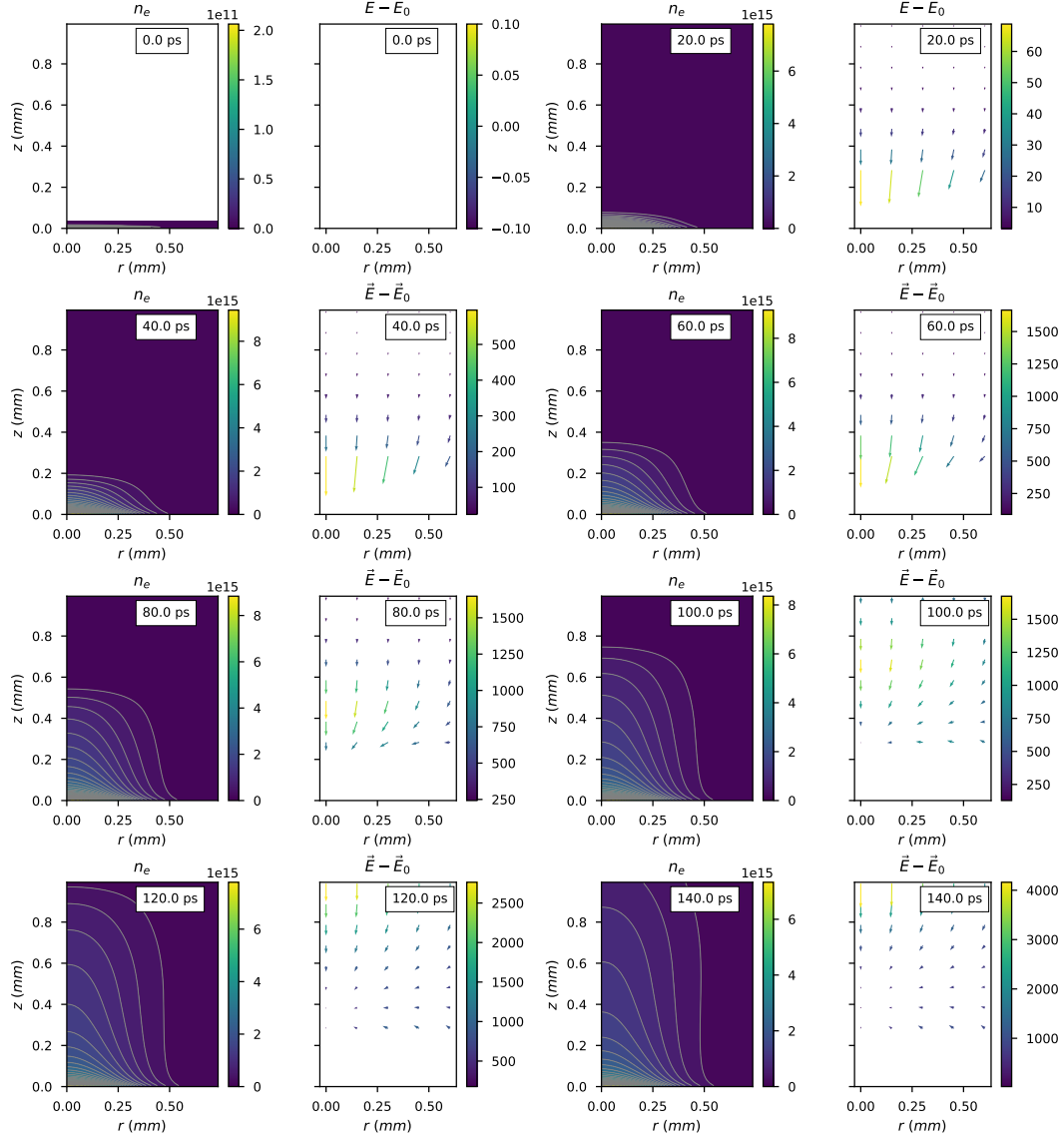


Figure 3: Evolution of the electron density and electric field perturbation from when electrons are first released from the cathode at  $t = 0$  (top right) to when a steady state flow is reached near  $t = 140$  ps. At all times, the highest electron density is near the cathode, and drops off quickly as we move across the gap. This simulation is done on a  $160 \times 160$  grid and uses a Gaussian profile with half width half maximum of  $HWHM = 0.2$  mm for electron emission.

we need to either achieve a greater perturbation or use a more precise voltage source.

There are a number of parameters we could consider varying to discover a more reliable trigger, including gap geometry, pulse power, and pulse width. Here, we only consider pulses with a variety of width parameters because this is a change we can easily make to a physical experiment and we can easily explore numerically. Specifically, we compare results from the three electron number density boundary conditions in Figure 1.

As shown in Figure 4, tighter profiles result in marginally greater electric field perturbations as well as the greatest number of electrons available to seed a discharge on the axis of symmetry near the anode, where the electric field perturbation is greatest. Both of these two properties are desirable for triggering the spark gap. From a design perspective, we evidently want to achieve as tight a focus of the light as possible.

In Figure 4, we can also see that it takes roughly  $\sim 150$  ps for the maximum perturbed electric field to be reached regardless of the beam width. This poses a fundamental limit on the timing jitter that a UV-light triggered spark gap can achieve. To see this, suppose that we have a gap in which the uncertainty in the applied electric field is exactly the same as the maximum electric field perturbation that we can achieve with our UV-light trigger. Then, if we hold the spark gap just below its breakdown threshold, the field perturbation required to discharge the gap will range from almost nothing to the maximum field perturbation possible. Thus, if we had an otherwise ideal spark gap which discharged exactly when its threshold was reached, it would have a timing jitter limited by the time it takes for the maximum field perturbation to be reached.

In the event this were the dominant jitter source, we could improve the trigger by decreasing the time it takes for the maximum perturbation to be reached. This can be done by increasing the speed of the electron cloud, which can be achieved: by increasing the applied electric field so as to increase the electrostatic force on electrons; by increasing the velocity of photo-electrons by decreasing the work function of the cathode or increasing the energy of incident photons; or by decreasing the ambient pressure of the gap so as to decrease the drag on the electron cloud.

## 4 Conclusion

In this thesis, I model the pre-breakdown dynamics of an electron cloud in a proposed UV-light triggered spark gap. To trigger this spark gap, we hold it just below its breakdown voltage; then, we shine UV-light on the cathode which forms an electron cloud. We have shown that the electron cloud perturbs the applied electric field near the anode. Based off similar situations, such as simulations done by Sun et. Al [1], we know a streamer should grow from any point where the electric field locally exceeds the breakdown field of a spark gap. We conclude that UV-light will consistently trigger a spark gap so long as the perturbation caused by the electron cloud is larger than the uncertainty in the applied electric field.

In previous experiments, we succeeded in occasionally triggering a spark gap so that the gap would discharge only when UV-light was directed onto the cathode, but we failed to trigger the spark gap consistently. The results of this thesis indicate that the inconsistency in our trigger is due to the electric field perturbation being smaller than the uncertainty in the applied electric field. We have shown that by achieving a tighter focus of the incident light on the cathode, decreasing the

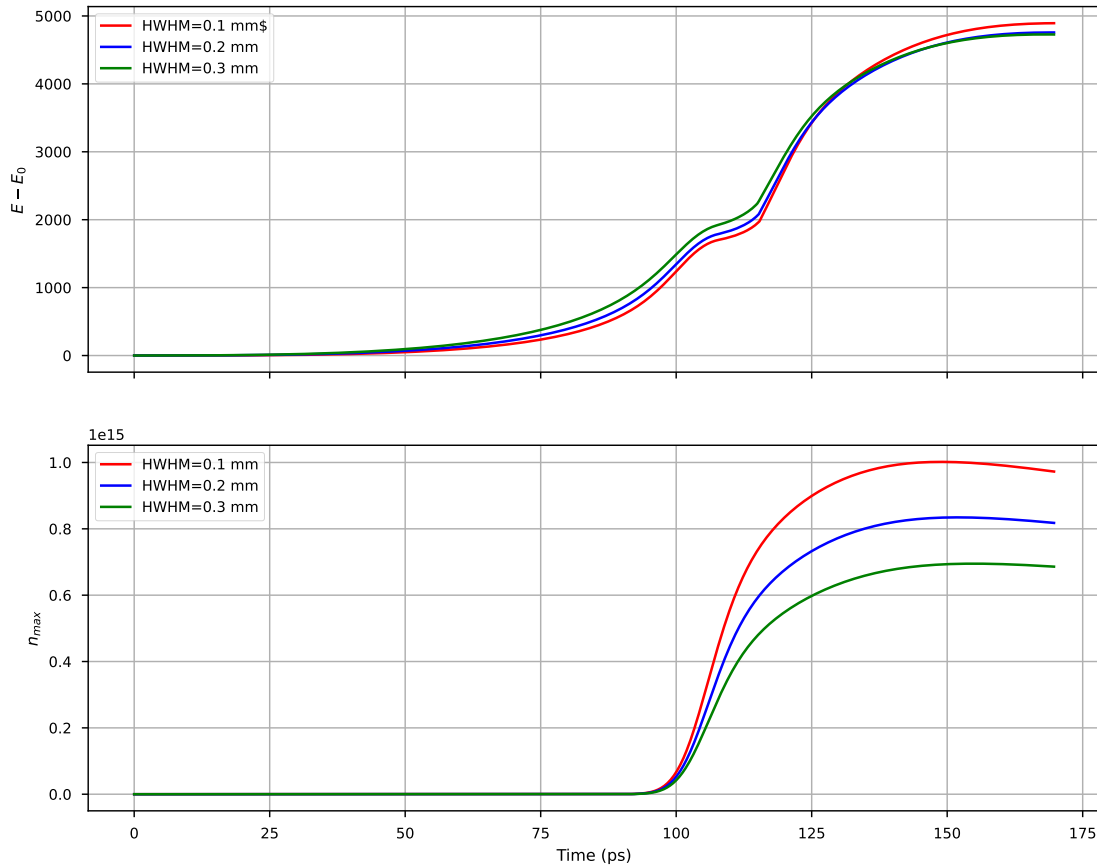


Figure 4: Here, we show the maximum electric field perturbation (top) and maximum electron number density (bottom) near the anode as each simulation evolves in time. We can see that the narrowest electron confinement ultimately results in the greatest electric field perturbation, although the difference is marginal. More importantly, the narrowest electron confinement results in the greatest electron number density at the anode, meaning there are more electrons available to seed a discharge.

uncertainty in the applied electric field, or increasing the power of incident light, we can create a more consistent trigger mechanism for our UV-light triggered spark gap. In future experiments, we will test these ideas in the laboratory and apply the results to the design of a UV-light triggered spark gap as an economical, low jitter high voltage pulse generator.

## Acknowledgements

Thank you to Dr. Adam Light for introducing me to this topic, providing valuable discussion throughout the research process, and giving extensive feedback on this manuscript.

## Source Code and Data Availability

Source code for the simulation framework used in this thesis is available online at [https://github.com/3-3-3/Prebreakdown\\_Dynamics/blob/main/Prebreakdown.py](https://github.com/3-3-3/Prebreakdown_Dynamics/blob/main/Prebreakdown.py). Data used in generating Figures in this thesis can be provided upon request.

## 5 Appendix A: Discretization and Solving Our Partial Differential Equations On a Computer

Although the detailed description of the numerical schemes used in our simulation are messy and of little physical interest, I provide them here for the interested reader. In this appendix, I derive finite difference equations for Poisson's Equation, the Electron Continuity Equation, and the Electron Momentum Equation. I also discuss the stability of our solutions.

We solve the partial differential equations derived in this thesis on a grid, and then update the electric potential, electron number density, and electron drift velocity at each grid point. So, to describe the solution, we describe how every grid point is updated as we move the simulation forward in time.

### 5.1 Poisson's Equation

Poisson's Equation<sup>13</sup> is given in terms of the electron number density  $n$  and the electron charge  $e$  as<sup>14</sup>:

$$\nabla^2 V = e \frac{n}{\varepsilon_0} \quad (11)$$

To solve this numerically for an arbitrary electron number density, we represent Poisson's Equation as the diffusion equation:

$$\frac{\partial V}{\partial t} = \nabla^2 V - \frac{e}{\varepsilon_0} n$$

Where  $t$  is not the simulation time, but rather an artificial parameter introduced to help solve Poisson's Equation at each time step of the simulation. In axis-symmetric cylindrical coordinates we represent this:

---

<sup>13</sup>see e.g. Chapter 2 of [8]

<sup>14</sup>In this section, we will revert to regular vector notation.

$$\frac{\partial V}{\partial t} = \frac{\partial^2 V}{\partial z^2} + \frac{1}{r} \frac{\partial}{\partial r} \left[ r \frac{\partial V}{\partial r} \right] - \frac{e}{\varepsilon_0} n$$

Which becomes exact as  $t \rightarrow \infty$  and  $\frac{\partial V}{\partial t} \rightarrow 0$ . Because we have no spatial first derivatives in this equation, a forward difference scheme for the time derivative and centered derivatives for the spatial derivatives will be stable [5], giving the following scheme:

$$\begin{aligned} \frac{V_{j,l}^{n+1} - V_{j,l}^n}{\Delta t} &= \frac{1}{\Delta z^2} \left[ V_{j+1,l}^n - 2V_{j,l}^n + V_{j-1,l}^n \right] \\ &\quad + \frac{1}{r_{j,l} \Delta r} \left[ \frac{r_{j,l+\frac{1}{2}}(V_{j,l+1}^n - V_{j,l}^n) - r_{j,l-\frac{1}{2}} * (V_{j,l}^n - V_{j,l-1}^n)}{\Delta r} \right] - \frac{e}{\varepsilon_0} n_{j,l}^n \end{aligned}$$

We can then use the stability condition  $\Delta t = \frac{\Delta r^2}{4} = \frac{\Delta z^2}{4}$  to end up with:

$$4V_{j,l}^{n+1} = V_{j+1,l}^n + V_{j-1,l}^n + \frac{r_{j,l} + \frac{\Delta r}{2}}{r_{j,l}} V_{j,l+1}^n + \frac{r_{j,l} - \frac{\Delta r}{2}}{r_{j,l}} V_{j,l-1}^n - \frac{e}{\varepsilon_0} n_{j,l}^n \Delta r \Delta z \quad (12)$$

For boundary conditions, the potential will be user specified at the anode, cathode, and at large  $r^{15}$ . The boundary at  $r = 0$  is tricky due to the singularity which occurs here. To deal with it, we consider our original diffusion equation in the limit as  $r \rightarrow 0$ :

$$\begin{aligned} \frac{\partial V}{\partial t} &= \frac{\partial^2 V}{\partial z^2} + \lim_{r \rightarrow 0} \left[ \frac{1}{r} \frac{\partial}{\partial r} \left[ r \frac{\partial V}{\partial r} \right] \right] - \frac{e}{\varepsilon_0} n \\ &= \frac{\partial^2 V}{\partial z^2} + \lim_{r \rightarrow 0} \left[ \frac{\partial^2 V}{\partial r^2} + \frac{1}{r} \frac{\partial V}{\partial r} \right] - \frac{e}{\varepsilon_0} n \\ &= \frac{\partial^2 V}{\partial z^2} + 2 \frac{\partial^2 V}{\partial r^2} - \frac{e}{\varepsilon_0} n \end{aligned}$$

Where L'Hôpital's Rule was used in the last step. Finite differencing this, we find that:

$$\frac{V_{j,0}^{n+1} - V_{j,0}^n}{\Delta t} = \frac{1}{\Delta z^2} \left[ V_{j+1,0}^n - 2V_{j,0}^n + V_{j-1,0}^n \right] + \frac{2}{\Delta r^2} \left[ V_{j,1}^n - 2V_j^n, 0 + V_{j,-1}^n \right] - \frac{e}{\varepsilon_0} n_{j,0}^n$$

By symmetry,  $V$  must be the same on each side of the  $r = 0$  boundary, so  $V_{j,l}^n = V_{j,-l}^n$ . Again using the stability condition  $\Delta t = \frac{\Delta r^2}{4} = \frac{\Delta z^2}{4}$ , we find that:

$$4V_{j,0}^{n+1} = 2V_{j,0}^n + 4V_{j,1}^n + V_{j+1,0}^n + V_{j-1,0}^n - \frac{e}{\varepsilon_0} n_{j,0}^n \Delta r \Delta z \quad (13)$$

And so we have described all boundaries and achieved a consistent scheme for our diffusion equation; we can then iteratively solve this to relax to a steady state solution for  $V$  and thus solve Poisson's Equation<sup>16</sup>.

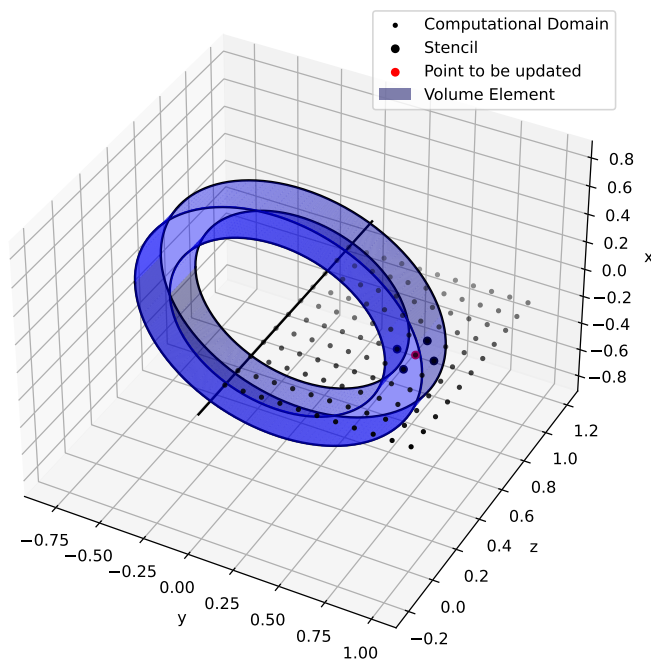


Figure 5: Here, we depict the 2D computational domain and corresponding 3D volume element used in solving our finite difference equations; we also show the stencil used to solve the Electron Continuity Equation and Electron Momentum Equation.

## 5.2 Electron Continuity Equation

The continuity equation comes from the assumption that electron density cannot be created or destroyed spontaneously, and so material entering one point in space must be coming from another point in space. In axis-symmetric cylindrical coordinates, our finite volume elements are concentric disks. If we center these volumes on one of our computational grid points, then adjacent points will be on the face of this volume; this is visualized in Figure 5. The electron flux across each face will be the product of the area of that face, the electron density at the face, and the normal component of the electron drift velocity at that face. The change in the electron density in this volume element is the total flux entering (or leaving) it divided by the volume of the element:

$$\frac{\Delta n_{j,l}}{\Delta t} = \frac{A_{j,l+1} u_{rj,l+1}^n n_{j,l+1}^n - A_{j,l-1} u_{rj,l-1}^n n_{j,l-1}^n}{V} + \frac{A_{j+1,l} u_{zj+1,l}^n n_{j+1,l}^n - A_{j-1,l} u_{zj-1,l}^n n_{j-1,l}^n}{V}$$

From geometry, we know our volume element is  $V = 2\pi(r_{j,l+1}^2 - r_{j,l-1}^2)\Delta z$ , while our area elements are  $A_{j,l+1} = 4\pi r_{j,l+1}\Delta z$ ,  $A_{j,l-1} = 4\pi r_{j,l-1}\Delta z$ ,  $A_{j+1,l} = A_{j-1,l} = \pi(r_{j,l+1}^2 - r_{j,l-1}^2)$ . Then, using a time centered leapfrog scheme:

$$\begin{aligned} \frac{n_{j,l}^{n+1} - n_{j,l}^{n-1}}{2\Delta t} &= \frac{2}{r_{j,l+1}^2 - r_{j,l-1}^2} [r_{j,l+1} u_{rj,l+1}^n n_{j,l+1}^n - r_{j,l-1} u_{rj,l-1}^n n_{j,l-1}^n] + \frac{1}{2\Delta z} [u_{zj+1,l}^n n_{j+1,l}^n - u_{zj-1,l}^n n_{j-1,l}^n] \\ n_{j,l}^{n+1} &= n_{j,l}^{n-1} + \frac{4\Delta t}{r_{j,l+1}^2 - r_{j,l-1}^2} [r_{j,l+1} u_{rj,l+1}^n n_{j,l+1}^n - r_{j,l-1} u_{rj,l-1}^n n_{j,l-1}^n] + \\ &\quad \frac{\Delta t}{\Delta z} [u_{zj+1,l}^n n_{j+1,l}^n - u_{zj-1,l}^n n_{j-1,l}^n] \end{aligned} \quad (14)$$

At the  $r = 0$  boundary, symmetry dictates that no net flux passes over the boundary. This leaves us with the following:

$$n_{j,0}^{n+1} = n_{j,0}^{n-1} + \frac{4\Delta t}{r_{j,1}} u_{rj,1}^n n_{j,1}^n + \frac{\Delta t}{\Delta z} [u_{zj+1,0}^n n_{j+1,0}^n - u_{zj-1,0}^n n_{j-1,0}^n] \quad (15)$$

At the anode, we want electron density to be absorbed, and similarly, at large  $r$ , we want density to pass out of the computational domain, so we choose diffuse boundary conditions in which normal spatial derivatives vanish. In one dimension, the method for achieving this is to set the value equal to adjacent points [6]. What I have done here is to do this in the direction normal to the boundary, but combine this with a step in the direction parallel to the surface, resulting in the following boundary conditions:

$$n_{j,L}^{n+1} = n_{j,L-1}^n - \frac{\Delta t}{\Delta z} [n_{j+1,L}^n u_{zj+1,L}^n - n_{j-1,L}^n u_{zj-1,L}^n] \quad (\text{at } r_{max}) \quad (16)$$

$$n_{J,l}^{n+1} = n_{J-1,l}^n - \frac{4\Delta t}{r_{l+1}^2 - r_{l-1}^2} [r_{l+1} n_{J,l+1}^n u_{rJ,l+1}^n - r_{l-1} n_{J,l-1}^n u_{rJ,l-1}^n] \quad (\text{at } z_{max}) \quad (17)$$

Which, along with a user specified boundary at the cathode, gives a consistent scheme for the electron continuity equation.

<sup>15</sup>Generally, large  $r$  is taken to approximate infinity so that the potential simply vanishes.

<sup>16</sup>Specifically, we use successive over relaxation—see Chapter 20 of [5] for details)

### 5.3 Electron Momentum Equation

We can write the Electron Momentum Equation in vector notation as:

$$\frac{\partial \vec{u}}{\partial t} + (\vec{u} \cdot \nabla) \vec{u} = -\frac{e}{m_e} \vec{E} - \nu_{en} \vec{u}$$

Where we take  $\vec{E} = -\nabla V$  to be the electric field. This results in the following equations for  $u_r$  and  $u_z$  in cylindrical coordinates<sup>17</sup>:

$$\begin{aligned}\frac{\partial u_r}{\partial t} &= -\frac{e}{m_e} E_r - u_r \frac{\partial u_r}{\partial r} - u_z \frac{\partial u_r}{\partial z} - \nu_{en} u_r \\ \frac{\partial u_z}{\partial t} &= -\frac{e}{m_e} E_z - u_r \frac{\partial u_z}{\partial r} - u_z \frac{\partial u_z}{\partial z} - \nu_{en} u_z\end{aligned}$$

We finite difference these using a leapfrog scheme (which uses both time centered derivatives and space centered derivatives). Thus, for interior points:

$$u_{rj,l}^{n+1} = u_{rj,l}^{n-1} - \frac{2e}{m_e} E_{rj,l}^n \Delta t - u_{rj,l}^n \frac{u_{rj,l+1}^n - u_{rj,l-1}^n}{\Delta r} \Delta t - u_{zj,l}^n \frac{u_{rj+1,l}^n - u_{rj-1,l}^n}{\Delta z} \Delta t - 2\nu_{en} u_{rj,l}^{n-1} \Delta t \quad (18)$$

$$u_{zj,l}^{n+1} = u_{zj,l}^{n-1} - \frac{2e}{m_e} E_{zj,l}^n \Delta t - u_{rj,l}^n \frac{u_{zj,l+1}^n - u_{zj,l-1}^n}{\Delta r} \Delta t - u_{zj,l}^n \frac{u_{zj+1,l}^n - u_{zj-1,l}^n}{\Delta z} \Delta t - 2\nu_{en} u_{zj,l}^{n-1} \Delta t \quad (19)$$

We use the old value of  $\vec{u}$  for the drag terms to maintain a stable solution. The electric field components are given by finite differencing the electric potential:

$$E_r = -\frac{V_{j,l+1}^n - V_{j,l-1}^n}{2\Delta r} \quad (20)$$

$$E_z = -\frac{V_{j+1,l}^n - V_{j-1,l}^n}{2\Delta z} \quad (21)$$

At the  $r = 0$  boundary, all derivatives with respect to  $r$  vanish due to symmetry, so:

$$u_{rj,0}^{n+1} = u_{rj,0}^{n-1} - u_{zj,0}^n \frac{u_{j+1,0}^n - u_{j-1,0}^n}{\Delta z} \Delta t - 2\nu_{en} u_{rj,0}^n \Delta t \quad (22)$$

$$u_{zj,0}^{n+1} = u_{zj,0}^{n-1} - \frac{2e}{m_e} E_{zj,0}^n \Delta t - u_{zj,0}^n \frac{u_{zj+1,0}^n - u_{zj-1,0}^n}{\Delta z} \Delta t - 2\nu_{en} u_{zj,0}^n \Delta t \quad (23)$$

Similarly,  $r = r_{max}$  boundary, we assume that normal components of derivatives vanish so that:

$$u_{rj,L}^{n+1} = u_{rj,L}^{n-1} - u_{zj,L}^n \frac{u_{rj+1,L}^n - u_{rj-1,L}^n}{\Delta z} \Delta t - 2\nu_{en} u_{rj,L}^n \Delta t \quad (24)$$

$$u_{zj,L}^{n+1} = u_{zj,L}^{n-1} - \frac{2e}{m_e} E_{zj,L}^n \Delta t - u_{zj,L}^n \frac{u_{zj+1,L}^n - u_{zj-1,L}^n}{\Delta z} \Delta t - 2\nu_{en} u_{zj,L}^n \Delta t \quad (25)$$

<sup>17</sup>We use  $(A \cdot \nabla)_r = A_r \frac{\partial B_r}{\partial r} + \frac{A_\phi}{r} \frac{\partial B_r}{\partial \phi} + A_z \frac{\partial B_r}{\partial z} - \frac{A_\phi B_\phi}{r}$ ,  $(A \cdot \nabla)_\phi = A_r \frac{\partial B_\phi}{\partial r} + \frac{A_\phi}{r} \frac{\partial B_\phi}{\partial \phi} + A_z \frac{\partial B_\phi}{\partial z} + \frac{A_\phi B_r}{r}$ , and  $(A \cdot \nabla)_z = A_r \frac{\partial B_z}{\partial r} + \frac{A_\phi}{r} \frac{\partial B_z}{\partial \phi} + A_z \frac{\partial B_z}{\partial z}$  [10] under axisymmetry to arrive at equations for  $u_r$  and  $u_z$ .

We make a similar assumption at the anode ( $z = z_{max}$ ) so that:

$$u_{rJ-1,l}^{n+1} = u_{rJ-1,l}^{n-1} - \frac{2e}{m_e} E_{rJ-1,l}^n \Delta t - u_{zJ-1,l}^n \frac{u_{rJ-1,l+1}^n - u_{rJ-1,l-1}^n}{\Delta r} \Delta t - 2\nu_{en} u_{rJ-1,l}^n \Delta t \quad (26)$$

$$u_{zJ-1,l}^{n+1} = u_{zJ-1,l}^{n-1} - \frac{2e}{m_e} E_{zJ-1,l}^n \Delta t - u_{rJ-1,l}^n \frac{u_{zJ-1,l+1}^n - u_{zJ-1,l-1}^n}{\Delta r} \Delta t - 2\nu_{en} u_{zJ-1,l}^n \Delta t \quad (27)$$

Where we stop the scheme at  $J - 1$  rather than  $J$  so that  $\vec{E}$  is defined at the boundary. Similarly, at the  $z = 0$  boundary, we simply use the interior scheme for both  $u_{r1,j}$  and  $u_{z1,j}$  while taking  $u_{r0,j} = 0$  always and allowing  $u_{z0,j}$  to be described by a boundary function (generally a constant typical of an electron emitted from a metal surface via the photoelectric effect). Corner points are taken to be combinations of the above conditions, giving the full consistent scheme for the electron momentum equation.

## 5.4 Stability

To obtain a stable solution—a solution where the error does not grow without bound—we use the CFL condition:

$$\Delta t \leq \frac{1}{4} \max_{j,l \in \{J,L\}} \left( \frac{1}{\sqrt{\left(\frac{u_{zj,l}^n}{\Delta z}\right)^2 + \left(\frac{u_{rj,l}^n}{\Delta r}\right)^2}} \right) \quad (28)$$

This condition asserts that  $\Delta t$  must be less than the time it takes for the fluid to flow a grid point to adjacent grid points (the factor of 4 is a geometrical factor applying to 2D).

Unfortunately, the CFL condition does not guarantee stability, and in our case is insufficient to maintain a stable solution. A well known problem which arises when using the cell-centered and time-centered finite difference schemes we employ when solving the Continuity Equation and the Electron Momentum Equations is that they are prone to so called mesh drift instabilities. To understand these instabilities, we define even cells to be those where  $j + l$  is even and odd cells to be those where  $j + l$  is odd. Then, by inspecting our scheme for the Continuity Equation or the Electron Momentum Equation, we can see that when we update an even cell, we only reference odd cells, and vice versa. This allows for small discrepancies between the even grid and the odd grid to grow, resulting in an unstable solution.

To avoid these instabilities, we need to couple the two grids. While there are a number of methods for accomplishing this, we implemented an averaging of the two grids at each step of the simulation. Specifically, we convolve our solution with a Gaussian profile having a width of roughly a grid space<sup>18</sup>, which is sufficient to obtain stable solutions.

## 5.5 Computational Complexity

In the Section 3 we discuss the error in our simulated solutions on a number of grid sizes. Because we do seem to converge to a solution as we increase the grid size, in principle we can continue to reduce

---

<sup>18</sup>We used the gaussian\_filter method available in scipy.ndimage package.

numerical error to acceptable levels by increasing the number of grid points. However, in practice the time it takes to run a simulation places an upper limit on how effective this strategy can be.

In terms of run time, the main computational bottleneck is the relaxation algorithm used in resolving the electric potential. Consider an  $N \times N$  grid. The number of computations per relaxation iteration will be  $O(N^2)$ : we do one roughly identical calculation per grid point. Then, we can see that the artificial time step used in the relaxation algorithm is proportional to the grid spacing squared, so the number of iterations required to relax to a solution to Poisson's Equation will scale roughly as  $O(N^2)$ . Finally, the CFL condition dictates that  $\Delta t$  is proportional to the grid spacing, so the number of steps the simulation requires to simulate the same amount of time on different grids scales as  $O(N)$ . Putting this altogether, we can see that our simulation is at least  $O(N^5)$ , so, unless we were to devote significantly more resources or time to the simulation, we will be unable to achieve significantly more accurate results without algorithmic adjustments.

## References

- [1] Anbang Sun et al., *J. Phys. D: Appl. Phys.* 47 445205 (2014).
- [2] Sander Nijdam et al., *Plasma Sources Sci. Technol.* 29 103001 (2020).
- [3] D.E. Neuenschwander, *Emmy Noether's Wonderful Theorem*, 2nd ed. (John Hopkins University Press, Baltimore, 2017).
- [4] P.M. Bellan, *Fundamentals of Plasma Physics*, (Cambridge University Press, United Kingdom, 2006).
- [5] W. H. Press, S. A. Teukosky, W. T. Vetterling, and B. P. Flannery, 3rd ed. *Numerical Recipes: The Art of Scientific Computing*, (Cambridge University Press, United Kingdom, 2007).
- [6] J. Franklin, *Computational Methods For Physics*, (Cambridge University Press, United Kingdom, 2013).
- [7] Private correspondence with Adam Light.
- [8] D. J. Griffiths, *Introduction to Electrodynamics*, 4th ed. (Cambridge University Press, United Kingdom, 2017).
- [9] B. Bagheri et al., *2018 Plasma Sources Sci. Technol.* 27 095002
- [10] A.S. Richardson, *2019 NRL Plasma Formulary*, (Naval Research Laboratory, 2019).
- [11] G.K. Batchelor, *An Introduction to Fluid Dynamics*, (Cambridge University Press, 1970).
- [12] M. G. Hogg, I. V. Timoshkin, S. J. MacGregor, M. P. Wilson, M. J. Given and T. Wang, "Electrical breakdown of short non-uniform air gaps," 201319th IEEE Pulsed Power Conference (PPC), San Francisco, CA, USA, (2013), pp. 1-4, doi: 10.1109/PPC.2013.6627482.
- [13] A. M. Darr, C. R. Darr, A. L. Garner, *Physical Review Research* 2 033137 (2020).